

Use of Alloying to Effect an Equiaxed Microstructure in Additive Manufacturing and Subsequent Heat Treatment of High-Strength Titanium Alloys



BRIAN A. WELK, NEVIN TAYLOR, ZACHARY KLOENNE, KEVIN J. CHAPUT, STEPHEN FOX, and HAMISH L. FRASER

This paper addresses the use of alloying additions to titanium alloys for additive manufacturing (AM) with the specific objective of producing equiaxed microstructures. The additions are among those that increase freezing ranges such that significant solutal undercooling results when combined with the rapid cooling rates associated with AM, and so be effective in inducing a columnar-to-equiaxed transition (CET). Firstly, computational thermodynamics has been used to provide a simple graphical means of predicting these additions; this method has been used to explore additions of Ni and Fe to the alloy Ti-6Al-4V (Ti64). Secondly, an experimental means of determining the minimum concentration of these alloying elements required to effect the CET has been developed involving gradient builds. Thirdly, it has been found that additions of Fe to Ti64 cause the alloy to change from an α/β Ti alloy to being a metastable β -Ti alloy, whereas additions of Ni do not produce the same result. This change in type of Ti alloy results in a marked difference in the development of microstructures of these compositionally modified alloys using heat treatments. Finally, hardness measurements have been used to provide a preliminary assessment of the mechanical response of these modified alloys.

<https://doi.org/10.1007/s11661-021-06475-3>
© The Author(s) 2021

I. INTRODUCTION

THERE has been considerable recent interest in the literature regarding the application of Additive Manufacturing (AM) to the production of (near) net-shape components of metallic alloys.^[1,2] Among various structural metallic materials, Ti alloys have received much attention, not only because of the attractive aspects of this processing route, but also because the as-printed high-performance Ti alloys processed by AM tend to be free of cracks.^[3] There is, however, a disadvantage associated with the AM of such alloys, namely, the tendency to form coarse columnar grains, aligned in the build direction. These coarse grains do not resemble optimized microstructures for high-performance applications, and also impart considerable texture to the

as-printed components,^[4,5] which drives asymmetric mechanical responses, not typically desired. There appear to be four approaches which have been employed in attempts to avoid undesirable microstructural features in the AM-deposited alloys. The first has involved the use of variations in processing parameters to enable a point heat source to control microstructure, such as in the alloy IN-718^[6]; this means of microstructure control is rather time consuming. The second approach makes use of additions of inoculants to control solidification, such as those used in the optimization of microstructure in high-strength Al alloys.^[7] This approach has been demonstrated in Ti alloys with the addition of boron as well as lanthanum, however, an issue of formation of intermetallic compounds arises which may limit mechanical properties, specifically in fatigue.^[8,9] The third approach uses alloying additions to effect a change of solidification mode. An example of this method involves peritectic Ti alloys for 3D printing.^[10] In this example, Ti-La and Ti-Fe-La alloys were printed, and the resulting microstructures consist of elongated and tortuous α grains with some refined equiaxed grains. The fourth approach uses dilute alloying additions to produce an equiaxed grain morphology. The role of the dilute additions is to increase the freezing range of Ti alloys in order to promote solutal undercooling, which, combined with the fairly

BRIAN A. WELK, NEVIN TAYLOR, ZACHARY KLOENNE, and HAMISH L. FRASER are with the Center for the Accelerated Maturation of Materials, Department of Materials Science and Engineering, The Ohio State University, Columbus, OH 43212 USA. Contact e-mail: fraser.3@osu.edu KEVIN J. CHAPUT is with the Aerospace Systems, Northrop Grumman Corporation, Melbourne, FL 32901 USA. STEPHEN FOX is with the Henderson Technical Laboratory, Titanium Metals Corporation, Henderson, NV 89015 USA.

Manuscript submitted February 24, 2021, accepted September 27, 2021.

Article published online October 25, 2021

Table I. Source and Size Ranges of the Powders Obtained for This Study

	Supplier	Size (μm)
CP-Ti	ATI Powder Metals	– 149/+ 44
Ti64	ATI Powder Metals	– 149/+ 44
Ti18	TIMET Powder Metals	– 149/+ 44
Fe	Atlantic Equipment Engineers	– 149
Ni	Alfa Aesar	– 149/+ 44
Mo	Alfa Aesar	– 88

The composition of the alloy Ti18 is Ti–5.5Al–5V–5Mo–2.4Cr–0.75Fe–0.15O.

rapid cooling rates associated with AM, may result in a CET. Hunt, as well as many others, has demonstrated the importance of an increased freezing range in the growth of equiaxed grains.^[11,12] A number of reports of the results of adding such solute additions may be referenced. Thus, for example, it has been reported that alloying with β -eutectoid stabilizers at sufficient concentrations results in an equiaxed microstructure during laser deposition of powders.^[13] In that work, the choice of eutectoid stabilizers was based on the increase in freezing range accompanying the addition of these elements to Ti. In a more recent report, Zhang *et al.* investigated copper as an alloying element in pure titanium to achieve fine equiaxed grains during additive manufacturing.^[14] Copper was selected as an alloying element due to its ability to provide constitutional undercooling during solidification based on the growth restriction theory developed from castings. This theory, as referenced from the earlier work of Birmingham *et al.*,^[15] identifies solutes with a growth restriction factor, Q , in binary Titanium alloys that will promote finer equiaxed grain sizes. The intermetallic formation of Ti_2Cu occurs rapidly below 792 °C and cannot be suppressed with water quenching. This prevents the use of heat treatment to produce microstructures in the Ti–Cu alloys that would not contain these intermetallic compounds. In another recent paper, Simonelli *et al.* investigated alloying with iron to reduce the typical anisotropy found in Ti–6Al–4V (Ti64) in laser powder-bed fusion.^[16] Iron was selected as an alloying element based on the same rationale as used to identify copper as a potential alloying element due to its growth restriction factor Q , combined with a relatively high solubility in the beta-phase. Iron was also selected as an alloying element to Ti–6Al–4V due to the lack of brittle intermetallic formation that accompanies many other solute additions. Thus, while thermodynamics dictate a TiFe intermetallic should appear in the Ti–Fe alloy system, other factors involved in nucleation activation energy may be of a magnitude such that nucleation of this phase may be avoided or delayed. Reference was also made to research on Mo, Cr, B, La, and Y, which form unfavorable intermetallic compounds or insoluble particles that lead to undesirable microstructures.^[16] Regarding the use of β -isomorphous alloying elements, Mendoza *et al.*^[17] found that additions of ≈ 25 wt pct W resulted in refined microstructures during AM, but with a considerable increase in alloy density.

It appears that alloying additions to Ti alloys, which increase the alloys' freezing ranges, may be an effective method of inducing a CET during AM powder deposition, where it is the significant degree of undercooling prior to nucleation of β grains that can be achieved because of the large freezing range combined with the rapid cooling rates associated with AM. To be able to fully exploit this approach for *engineering* alloys, there are a number of issues that need to be addressed. Firstly, regarding the method itself, is it possible to employ computational thermodynamics, *e.g.*, CALPHAD or PANDAT, to identify those alloying additions that increase the freezing range of a given alloy? Secondly, while evidence has been presented in the papers to which reference has been made above that CETs do accompany the addition of a given alloying element, it has not been shown that the effects observed are due to alloying alone, and not due perhaps in part to other influences (*e.g.*, processing parameters and procedures). Thirdly, in terms of application of high-performance Ti components using this alloying method, it is not reasonable to expect that the as-printed parts will exhibit the appropriate microstructure for application. Thus, it is expected that while the presence of equiaxed grains will be an attractive feature, the distributions of the α and β phases, and possible intermetallic compounds (depending on the alloying addition), will need to be optimized by heat treatments. Hence, the response of these alloys to heat treatment will need to be assessed. The research upon which this paper is based was designed to address these various issues.

II. EXPERIMENTAL PROCEDURE

Pre-alloyed powders and compositionally graded alloys were deposited using a Directed Energy Deposition method, being an Optomec LENS™ system at The Ohio State University. The various powders used are listed in Table I. The OSU LENS™ system is equipped with an inert gas (Ar) glove box, two powder feeders, and an IPG 500 W fiber laser. Cylindrical specimens with a diameter of 10 mm were deposited with a laser power of 350 W (with a wavelength of 1.07 μm), a travel speed of 500 mm per minute, and oxygen content below 10 ppm. The scan strategy was continuous adjacent layering, rotating the scan 60 deg between adjacent layers. The hatch spacing was 0.38 mm, and the Z offset was 0.25 mm. To manufacture the compositionally graded alloys, the first powder feeder contained the

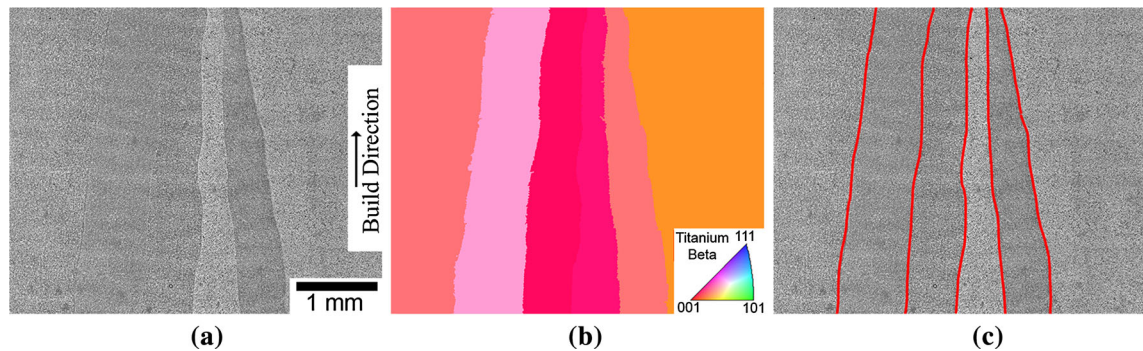


Fig. 1—(a) BSE image of the microstructure of a LENS™ build of CP-Ti, showing the elongated grains in the build direction; (b) IPF Map (EBSD) of the same area as in (a) showing the individual grains; (c) BSE image with the grain boundaries marked.

base alloy (*i.e.*, Ti64) and the second powder feeder contained a mixture of the modified alloy (*e.g.*, Ti64 + 5Fe); *all compositions are in wt pct*. The deposition began with the first powder feeder at 100 pct optimum flow rate and the second powder feeder at 0 pct optimum flow rate. During the deposition, the flow rate of the first powder feeder was reduced by 6.7 pct every 1 mm, while that of the second powder feeder was increased by 6.7 pct every 1 mm. The total height of the graded deposition was approximately 25 mm. Samples for microstructural characterization were sectioned parallel to the build direction.

As part of the heat-treatment study, buttons of desired compositions were produced using an arc-melter. The arc-melter was operated under a partial pressure of argon to avoid excessive aluminum evaporation. Each button was melted six times and was flipped after each melt to ensure homogeneity. When possible, master alloys were used as raw materials to reduce potential segregation.

Samples were prepared for hardness testing and microstructure characterization using traditional polishing procedures. Hardness measurements were conducted as specified in ASTM E18-20 for Rockwell C. An Instron machine was used with a 150 kgf major load, and the indenter was certified to a standard sample prior to each test. Microstructural characterization was performed using an Apreo (Thermo Fisher Scientific) scanning electron microscope (SEM), equipped with X-ray energy-dispersive spectroscopy (XEDS), and electron backscattered diffraction (EBSD) detectors. Regarding EBSD analyses, beta reconstruction was performed using the software developed by Pilchak.^[18] Samples for high-angle annular dark-field (HAADF) imaging on a (scanning) transmission electron microscope ((S)TEM) were prepared using a Nova Nano-Lab™ DualBeam FIB and examined in an aberration-corrected Titan³™ G2 60-300 (S)TEM. The characterization was conducted at the Center for Electron Microscopy and Analysis (CEMAS) at The Ohio State University.

Thermo-Calc 2020a was used to perform thermodynamic phase diagram calculations. The titanium database TCTI2 was selected, which includes the desired alloying elements. The intermetallic Ti₃Al was removed

from the diagrams because it was not found experimentally.

III. RESULTS AND DISCUSSION

A. Initial Observations

To illustrate the primary problem for which the current research has been undertaken, at first powders of CP-Ti have been deposited using LENS™ processing. A micrograph of the as-deposited material is shown in Figure 1. In Figure 1(a), a backscattered electron image recorded in the SEM is shown, yielding fairly weak contrast of coarse columnar grains aligned to the build direction. To confirm this observation, in Figure 1(b) an inverse pole figure (IPF) map obtained using EBSD confirms the coarse nature of the columnar grains, and Figure 1(c) shows the same image as in (a) but with the grain boundaries marked. It is this grain morphology that is considered to be somewhat disadvantageous compared with optimized microstructures for most structural applications of Ti alloys, and hence the need for the development of a solution, as described in the following.

B. Inducing a CET by Alloying

The primary metric used for identification of candidate alloying elements in this study was their impact on predicted freezing range. Thus, elements were selected that displayed an increased ability to widen the freezing range with limited solute additions. This follows the same phenomenological theory as growth restriction factors but is very simple to extend beyond binary titanium alloys such as in additions to Ti64. It should be noted that other more complex models for predicting a CET require thermophysical materials properties that are very difficult to obtain, and this is especially true for engineering alloys which typically contain a number of alloying elements. Thus, a CALPHAD approach is applied to investigate the impact of alloying elements on the solidification ranges. In Figures 2(a) and (b), the results of CALPHAD predictions on the variations in freezing ranges for the alloys Ti–Ni and Ti–Fe are

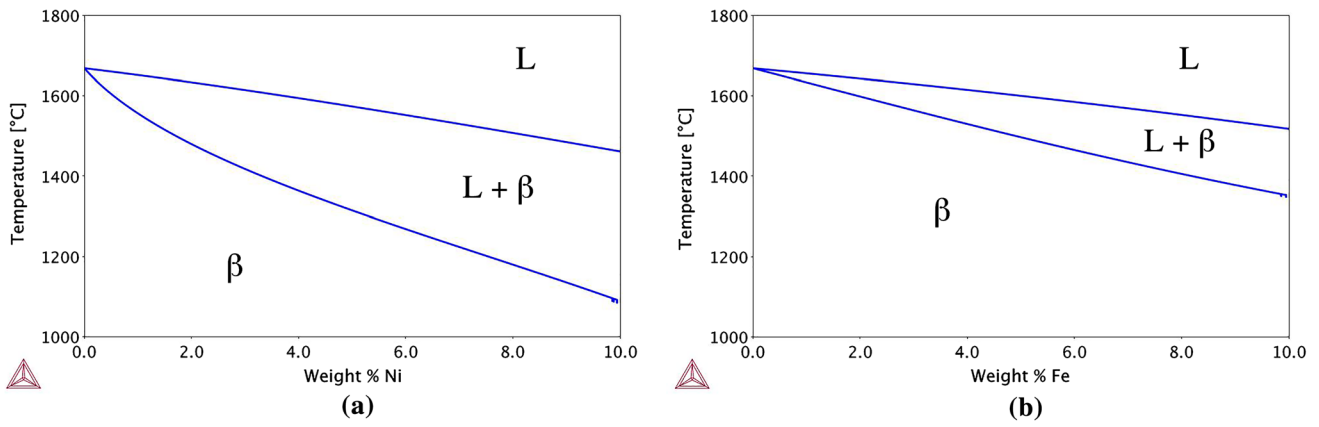


Fig. 2—Freezing ranges for alloys based on CP-Ti calculated using Thermo-Calc Software. (a) CP-Ti-Ni; (b) CP-Ti-Fe.

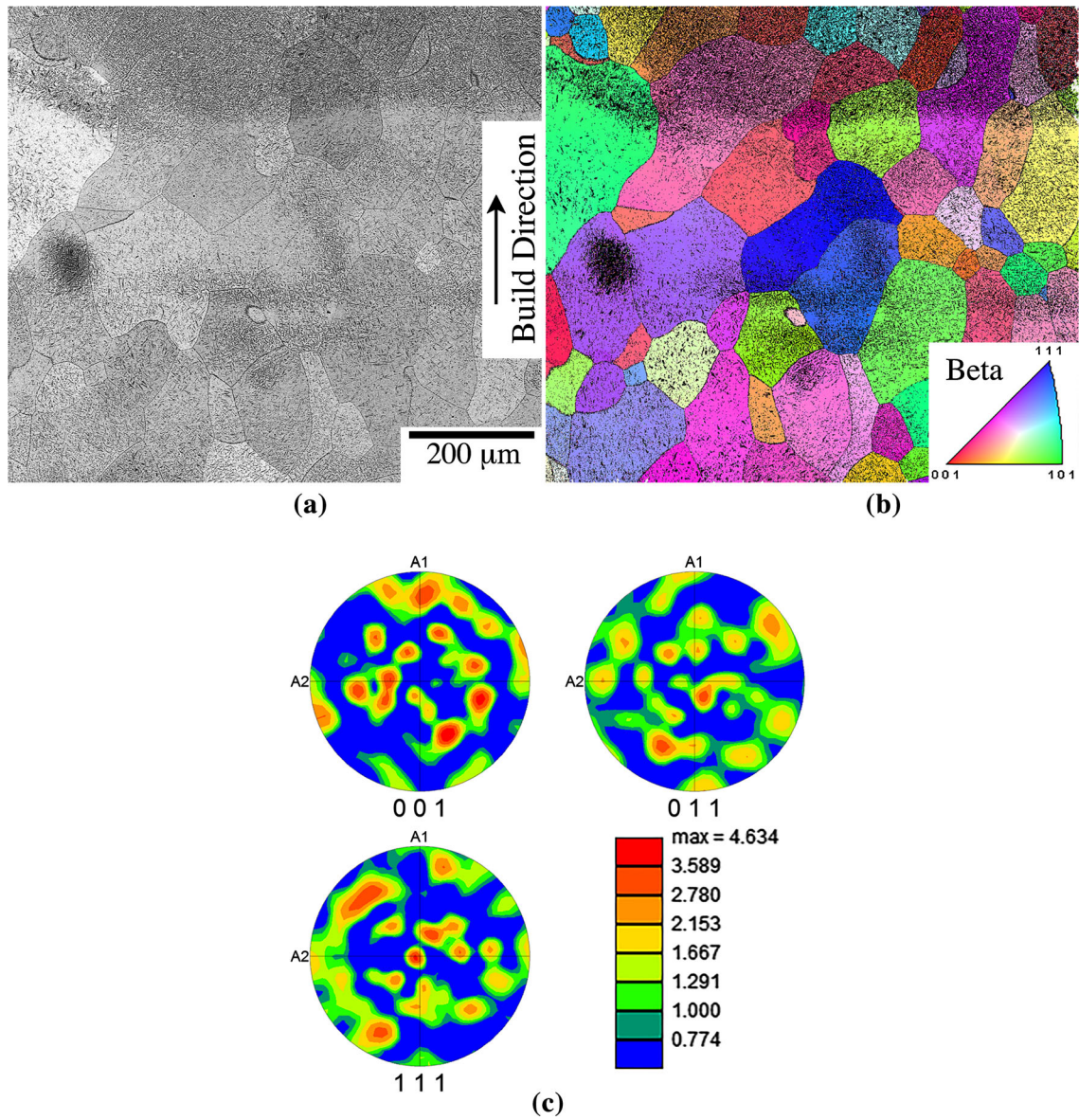


Fig. 3—Microstructure of a LENS™ build of CP-Ti with 6 pct Fe. The build direction is shown. (a) BSE image showing equiaxed grains; (b) EBSD-IPF map; (c) pole figures resulting from EBSD measurements showing a somewhat random texture.

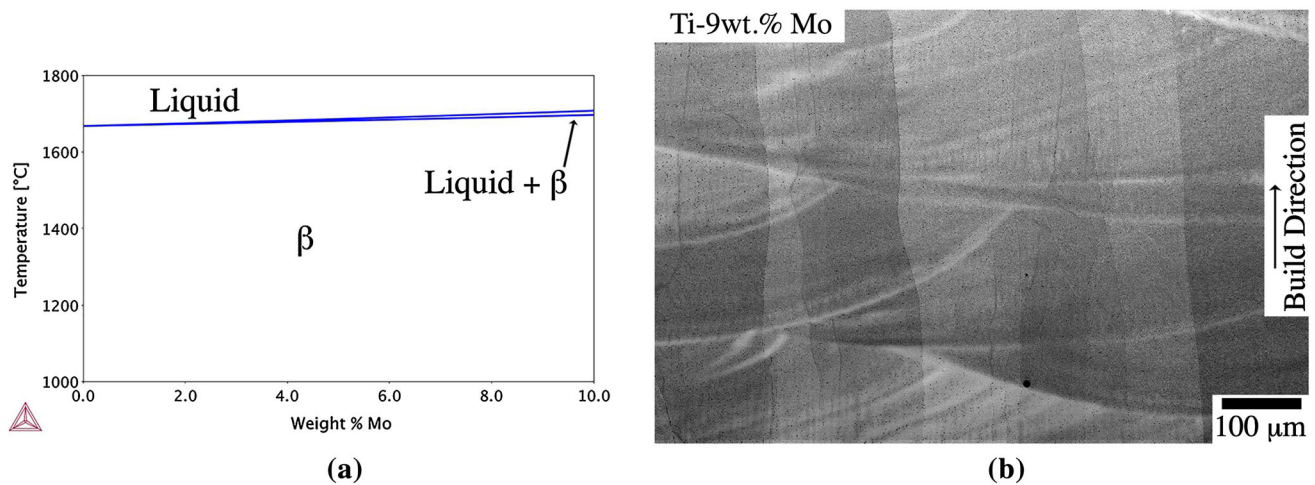


Fig. 4—(a) CALPHAD prediction of the variation in freezing range for binary CP-Ti–Mo alloys as a function of the addition of Mo. Note the increase in the freezing range is predicted to be very small; (b) BSE image taken from a LENSTM gradient build of Ti–Mo. The region shown corresponds to a composition of \approx Ti-9 pct Mo showing large columnar grains in the build direction (marked). This demonstrates that even at this composition of Mo, the columnar microstructure persists, and a CET has not been achieved.

shown, respectively. From these phase diagrams, it can be seen that both Ni and Fe increase the freezing range significantly, and so for these additions, it is predicted that they should be more prone to result in a CET during processing than the base alloy. These predictions have been validated experimentally. Thus, Figure 3(a) shows the typical microstructure of a LENSTM deposition of Ti–6Fe, where an equiaxed grain structure is produced in lieu of the columnar microstructure observed in Figure 1. This grain morphology may be seen clearly in the EBSD-IPF map shown in Figure 3(b), and pole figures deduced from these EBSD measurements show that the resulting texture is somewhat random (Figure 3(c)). The results for Ti–Ni (not shown here) are essentially the same, *i.e.*, the addition of Ni, which displays an increased predicted freezing range, also induced a CET during solidification. In contrast, in binary Ti–Mo alloys, CALPHAD predicts a very limited influence of this alloying element on the freezing range in binary Ti–Mo alloys (Figure 4(a)). Hence, based on this prediction, a typical columnar microstructure, similar to that of pure Ti, is expected in Ti–Mo binary alloys. This is indeed the case experimentally, where a coarse columnar microstructure is observed in the as-deposited Ti–9Mo, Figure 4(b).

The results for these binary alloys promote the effectiveness of using predicted freezing range alone as a simple metric to select alloying additions to effect a CET in AM (*i.e.*, with the attendant rapid rates of cooling). As stated above (Introduction), the simple method adopted here should also apply to the identification of additional alloying elements to Ti alloys that permit equiaxed microstructures to be realized in the as-deposited samples. To demonstrate the usefulness of this method, involving solute additions that increase the freezing range, CALPHAD predicted phase diagrams for the alloy Ti–6Al–4V (Ti64) with the addition of Ni and Fe, and the alloy TIMETAL 18 (Ti18: Ti–5.5Al–5V–5Mo–2.4Cr–0.75Fe–0.15O) with the

addition of Fe, are shown in Figures 5(a) through (c), respectively. As can be seen, the freezing ranges for each of these increase with alloying addition, and so based on the proposed metric, these elements should be strong candidates to increase the proclivity for a CET. This is shown to be the case experimentally. Thus, the coarse columnar microstructure of Ti64 as deposited using LENSTM is shown in weak contrast in Figure 6(a), with the grain structure confirmed in the IPF map shown in Figure 6(b), with the grain boundaries drawn in Figure 6(c). In contrast, the equiaxed microstructure in LENSTM of Ti64–3.5Ni is shown in Figure 6(d), with the IPF map (Figure 6(e)) and image with grain boundaries drawn in Figure 6(f). Both of these alloys were deposited in the same manner. These figures demonstrate the impact of Ni additions to promote an equiaxed microstructure in a base alloy of Ti64. It should be noted that in these gradient builds, for a given concentration of the solute addition, *e.g.*, Ni, the composition is uniform as shown in the XEDS maps provided in supplementary Fig. S-1 (refer to electronic supplementary material). A similar result is obtained when Fe additions to Ti18 are co-deposited using LENSTM. Thus, the coarse columnar microstructure of Ti18 as deposited using LENSTM is shown in Figure 7(a), and this may be compared with the equiaxed microstructure of Ti18–3Fe, similarly processed, in Figure 7(b). Based on these various results, it appears that the use of CALPHAD predicted phase diagrams of Ti alloys to establish whether given alloying additions cause increases in freezing ranges, and so induce a significant change in microstructure, *i.e.*, involving a CET, is a useful approach.

The method used here (*i.e.*, involving the influence of solute on freezing ranges) as well as those used in the references above^[14,16] are useful in determining which alloying elements may be used to induce a CET. However, these methods have not been developed to the point of being able to predict the *minimum* amount of a given alloying element that would result in a CET in

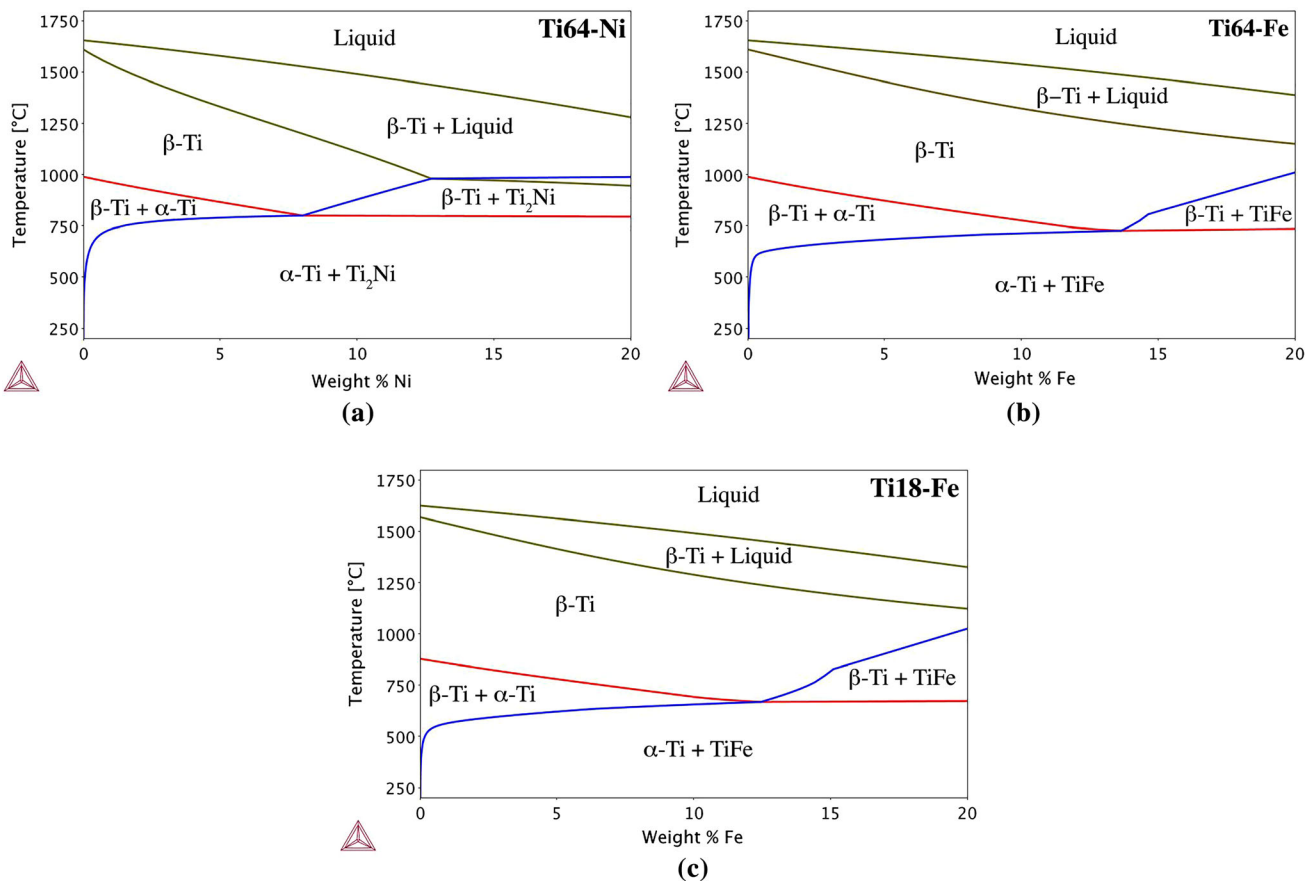


Fig. 5—Pseudo-binary phase diagrams calculated using Thermo-Calc Software: (a) Ti64–Ni; (b) Ti64–Fe; (c) Ti18–Fe.

the as-deposited AM samples. It is important that this quantity be determined since, as will be discussed below, there are other microstructural consequences to the use of alloying elements in amounts above solubility limits in the solid state. An experimental method of determining this minimum amount of an alloying element is described in the following. It is possible using a laser-based direct metal deposition technique, such as LENSTM, to build samples in which a gradient in composition may be developed, an early example of this being described in Reference 19. This gradient approach may be used to build alloys with increasing concentrations of alloying elements where the transition from columnar to equiaxed grain morphology may be determined by direct observation. Consider the gradient build of Ti64 with increasing additions of Ni as shown in Figure 8(a). As may be observed, the columnar-to-equiaxed transition occurs at approximately 3Ni; the composition is determined following deposition using XEDS in the SEM. In this experiment, once the Ni concentration reached approximately 7 pct, the concentration of Ni was then reduced as the build continued. As can be seen, Figure 8(b), an equiaxed-to-columnar transition (ECT) occurred at about 3Ni. It appears then that the CET and ECT are induced only by the concentrations of the alloying addition. From these gradient experiments, it may be determined that the minimum concentration of Ni required to produce a

CET using this AM processing procedure in Ti64 is $\approx 3\text{Ni}$. This experiment involving gradient builds has been repeated for the case of Ti18 with Fe additions. The result is shown in Figure 8(c), where the CET occurs also at about 3Fe, defining this as the minimum amount of Fe required for the CET. Consideration of the influence of other alloying additions to Ti alloys regarding microstructural modifications, *i.e.*, by use of CALPHAD predictions of phase diagrams, it is found that, in the main, β -eutectoid stabilizing elements are predicted to be effective in causing a CET.

C. Metallurgical Consequences of Additions of β -Eutectoid Elements to Existing Ti Alloys

As was noted above, the necessary quantities of these β -eutectoid additions to Ti alloys to effect a CET are expected to be above the solubility limits of Ti solid solutions, and so it is important to assess the influences of possible solid-state precipitation reactions that may occur during processing. In view of these possible phase transitions, it is necessary to examine the use of heat treatments that may be employed to optimize the microstructures of these modified versions of Ti alloys, after the additive build. Consider first the as-deposited microstructures in alloys with the minimum amount of alloying addition that has been determined by the gradient experiment, described above, to effect a CET.

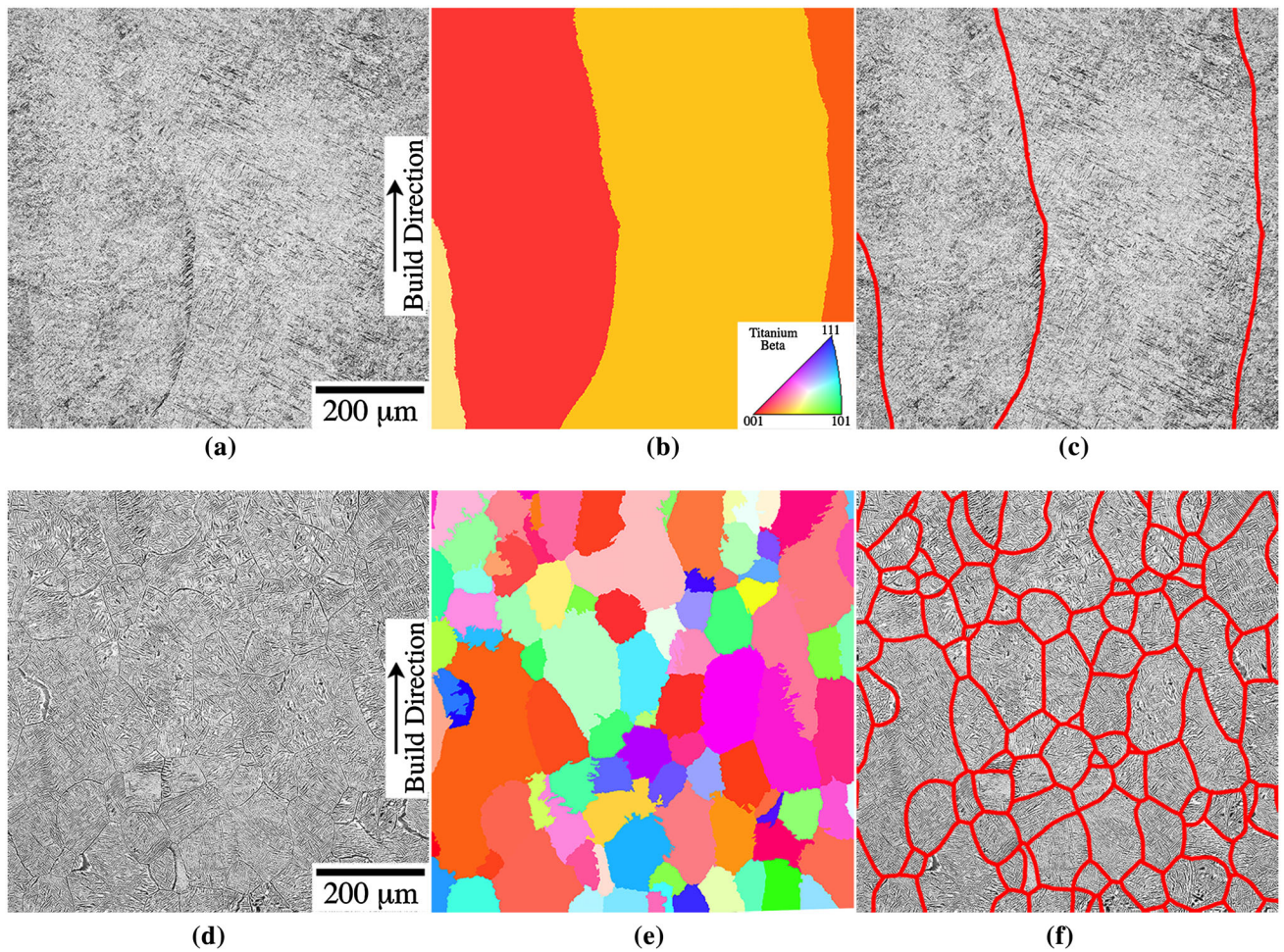


Fig. 6—BSE image of the microstructure of LENS™ builds: (a) The alloy Ti64 showing large columnar grains in the build direction; (b) IPF Map (EBSD) showing the grain structure of the same area as in (a); (c) same as in (a) but with the boundaries marked; (d) Ti64-3.5Ni showing the equiaxed nature of the grains; (e) IPF Map (EBSD) showing the grain structure of the same area as in (d); (f) same as in (d) but with the boundaries marked.

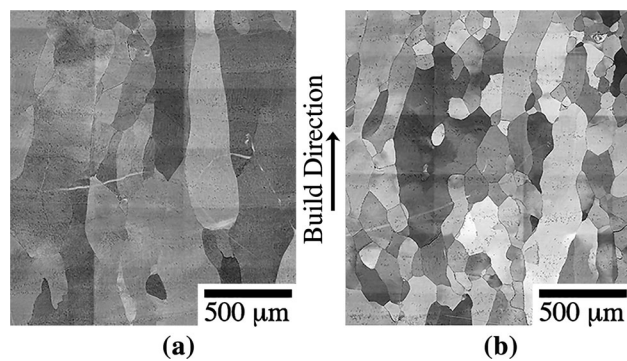


Fig. 7—BSE images of LENS™ deposits: (a) Ti18, exhibiting a coarse columnar microstructure; (b) Ti18 + \approx 3Fe, with an equiaxed grain morphology. The build direction is shown.

In Figures 9(a) and (b), the microstructures are shown of Ti64-3Ni and Ti64-3Fe, both the as-deposited using LENS™, respectively. It is clear that there is a considerable difference between these two microstructures. Thus, in the case of the Ni-containing deposit, the

microstructure consists of relatively large α laths that have precipitated in prior β grains. In addition to the α plates, there is also a distribution of the intermetallic compound, Ti_2Ni (its identity confirmed by XEDS analysis (not shown here)), as expected from the predicted phase diagram (Figure 5(a)). Evidently, there is sufficient driving force and diffusion to permit this precipitation to occur during LENS™ processing (perhaps aided by the re-heating that occurs during subsequent layer deposition of the build). Using MIPAR software (www.mipar.us), image analysis has been used to quantify the microstructure, where the volume fraction of the β phase is estimated to be \approx 18 pct and the average lath thickness is \approx 1.33 μm .

The microstructure of the as-deposited Ti64-3Fe (Figure 9(b)) stands in significant contrast. Thus, while there is a distribution of α laths in prior β grains, these are present on a much finer scale than those in the Ti64-3Ni alloy similarly processed. There is also no evidence of precipitation of the phase TiFe which, based on the CALPHAD predicted phase diagram (Figure 5(b)), at this concentration of Fe would be

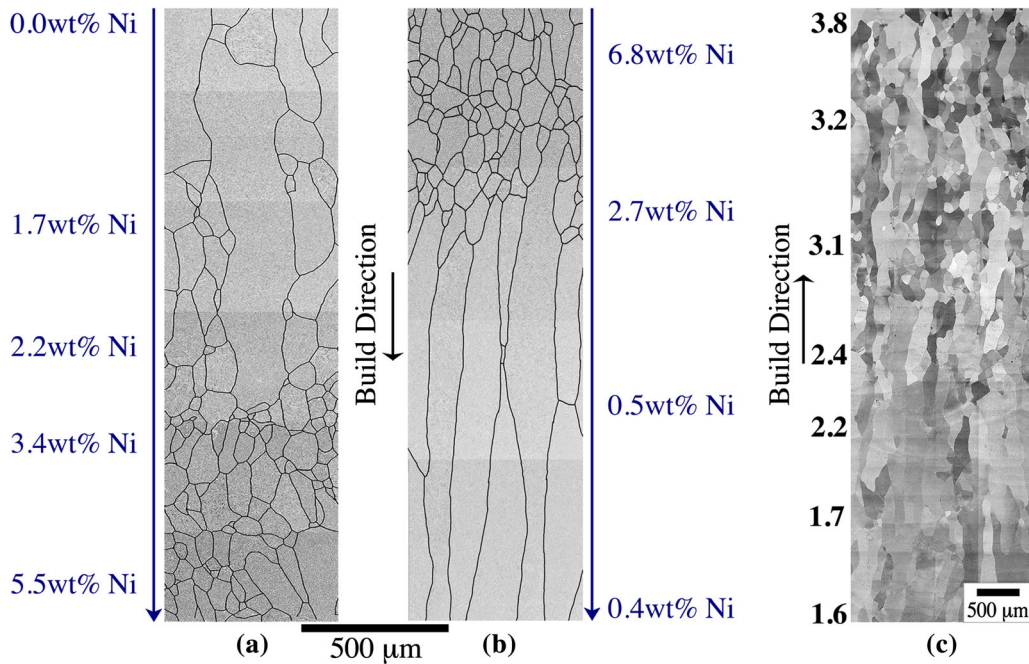


Fig. 8—BSE images of LENS™ gradient builds. (a) Ti64 with increasing Ni content from zero to ≈ 7 pct Ni; (b) continuing the LENS™ build but with decreasing amounts of Ni, reducing to essentially zero Ni content. The transition from columnar to equiaxed (a), and equiaxed to columnar (b) is clearly visible. (c) Ti18 with increasing concentrations of Fe (wt pct of additions shown in the figure).

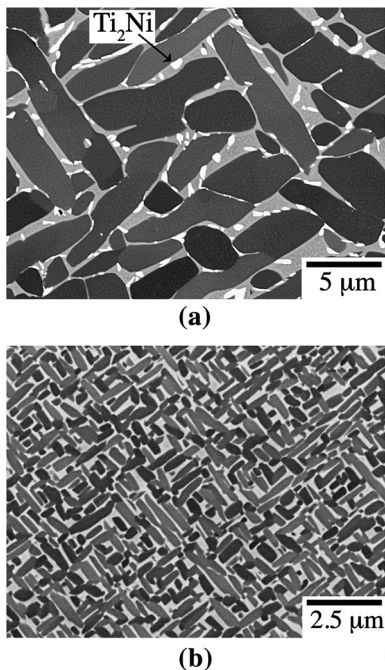


Fig. 9—Comparison of the as-deposited microstructures following LENS™ builds of (a) Ti64-3Ni, and (b) Ti64-3Fe. Note the presence of the intermetallic compound Ti_2Ni in the gradient build of Ti64-3Ni. Also note the rather different scale of the α plates.

expected to be in equilibrium with the α phase. Application of TEM to assess whether an intermetallic compound had formed on a scale that would not be observed in an SEM image revealed no such precipitation. Both Ni and Fe are known to diffuse very rapidly

in α -Ti,^[20] so the difference in the behavior between these two alloys regarding precipitation of intermetallic compounds is probably more due to other factors such as the difference in driving force for nucleation of the two intermetallic compounds, and the differences in nucleation barriers (*e.g.*, coherency). Using MIPAR software, image analysis has been used to quantify the microstructure of the Fe-containing alloy, with the following results: the volume fraction of the β phase is ≈ 30 pct and the average lath thickness is $\approx 0.15 \mu m$. The differences in the values of these various quantities between the two alloys are discussed below.

The possible development of the microstructure of these two alloys using heat treatments has been explored using arc-melted samples (note: it has been established that these alloys when arc-melted possess equiaxed microstructures, similar to the LENS™-deposited samples discussed above, refer to electronic supplementary S-2). Because of the similarity of the microstructures of samples processed by AM and arc-melting, the latter processing technique, being somewhat more efficient, was employed for this part of the study. Regarding the alloy Ti64-3Ni, the microstructure following solution heat treatment at $1000^\circ C$ for 1 hour, then water quenched to room temperature, is shown in Figure 10(a). As can be seen, this consists of refined laths following quenching. These are considered to be either α' martensite or refined α laths. In an attempt to establish their identity, XEDS experiments were performed on thin foils using an aberration-corrected STEM equipped with a ChemiSTEM detector (very large solid angle of detection) to determine if compositional differences were absent (*i.e.*, α' martensite), or were present (refined α laths); the results are shown in

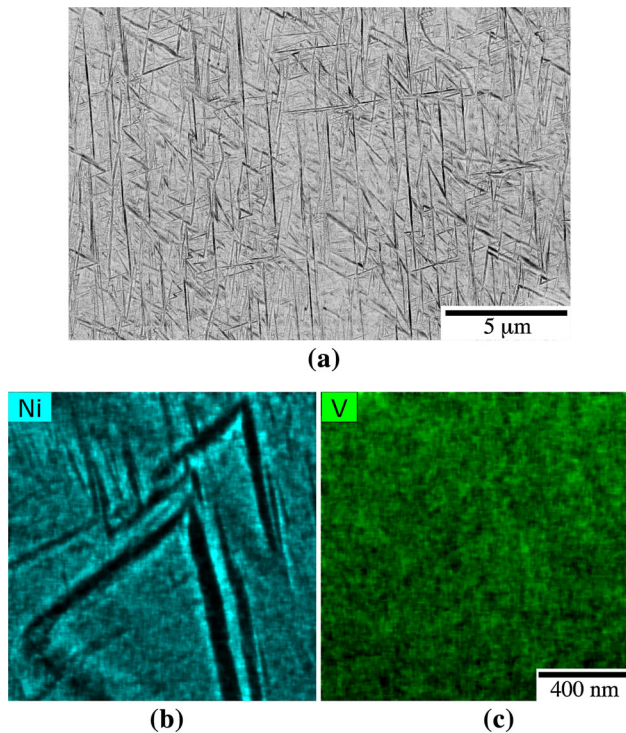


Fig. 10—Images of the microstructure of Ti64-3Ni following solution heat treatment at 1000 °C for 1 h, then water quenched to room temperature: (a) BSE image revealing the presence of thin laths following quenching; (b) STEM-XEDS map of the Ni distribution, revealing that during the quench, Ni has diffused out of the thin laths; (c) STEM-XEDS map of the V content, which is essentially randomly distributed, an observation in marked contrast to that of the Ni distribution.

the XEDS elemental maps shown in Figures 10(b) and (c). As can be seen in Figure 10(b), showing a map of the distribution of Ni, the element has partitioned from the laths to the surrounding β phase. This is a very surprising result as these samples have been quenched rapidly from the β phase (at 1000 °C), and hence, the diffusion of the Ni must have occurred during the quench. The elemental map for the element V (Figure 10(c)) is in marked contrast, with V being distributed more or less randomly. This result is consistent with the notion that Ni is a very fast diffuser in α -Ti [20]. From this result, it is tempting to speculate that the thin laths in Figure 10(a) are indeed not α' martensite, as there is a composition difference with the matrix (*i.e.*, β phase), although it is possible that α' martensite formed first with rapid diffusion of Ni from the martensitic laths producing the compositional differences observed. It is important to note that in the solution heat-treated and quenched samples, there is no evidence of the formation of Ti_2Ni .

These latter samples of Ti64-3Ni have been subjected to further heat treatments. Thus, following solution heat treatment and quenching to room temperature, samples were then aged for 1 hour at either 450 °C or 550 °C. The microstructure of the sample heat treated to 450 °C is shown in Figure 11(a), and this consists of a basketweave distribution of α plates in a β -Ti matrix. As can be seen, there is a bi-modal distribution of the

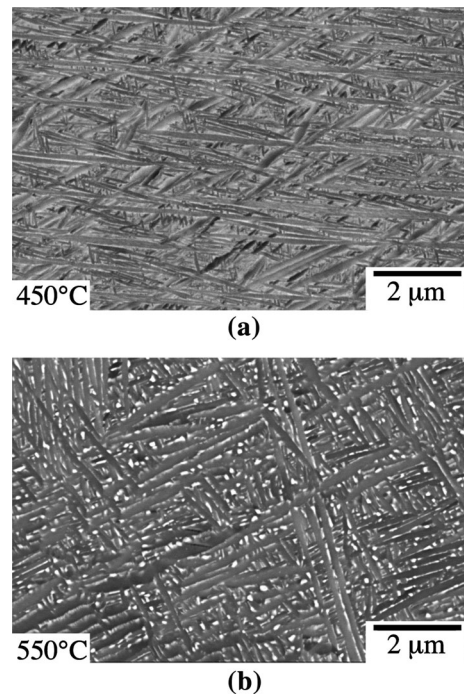


Fig. 11—BSE images of the microstructure of the alloy Ti64-3Ni. (a) and (b) Solution treated at 1000 °C for 1 h, followed by water quenching, and then aged for 1 h: (a) at 450 °C; (b) at 550 °C.

widths of α laths; the coarser laths are most probably coarsened versions of the refined laths formed during the quench (Figure 10), and the refined (secondary α) laths precipitated in the β phase, solute enriched by the rejection of Ni from the growing primary α laths. There is no evidence of precipitation of the intermetallic compound Ti_2Ni , or other phases, in this sample. In contrast, the microstructure of the sample aged at 550 °C, shown in Figure 11(b), exhibits thicker α laths (presumably because of the higher aging temperature), and also clear evidence for the precipitation of the intermetallic compound Ti_2Ni . Given the very rapid diffusion of Ni in Ti, as evidenced during quenching (Figure 10(b)), the stability of the microstructure against precipitation of the intermetallic phase when aging at 450 °C indicates that it may be possible to employ this alloy in applications requiring the basketweave microstructure close to intermediate temperatures.

The alloy Ti64-3Fe has also been subjected to solution heat treatment at 1000 °C for 1 hour, followed by quenching to room temperature. The resulting microstructure is shown in Figure 12(a) and consists of grains of the β phase. It appears that the refined α , or α' martensite, has been suppressed during quenching, and so by definition, the alloy may be considered to be a metastable β -Ti alloy [21]. Figures 12(b) and (c) are selected area diffraction patterns which show diffraction evidence for the presence of the ω and O' phases (the diffraction maxima are indicated in Figures 12(d) and (e), respectively). Both these phases represent metastabilities in the *bcc* lattice of the β phase; the ω phase is expected to be present in the β phase when the martensite transformation is frustrated, and the O'

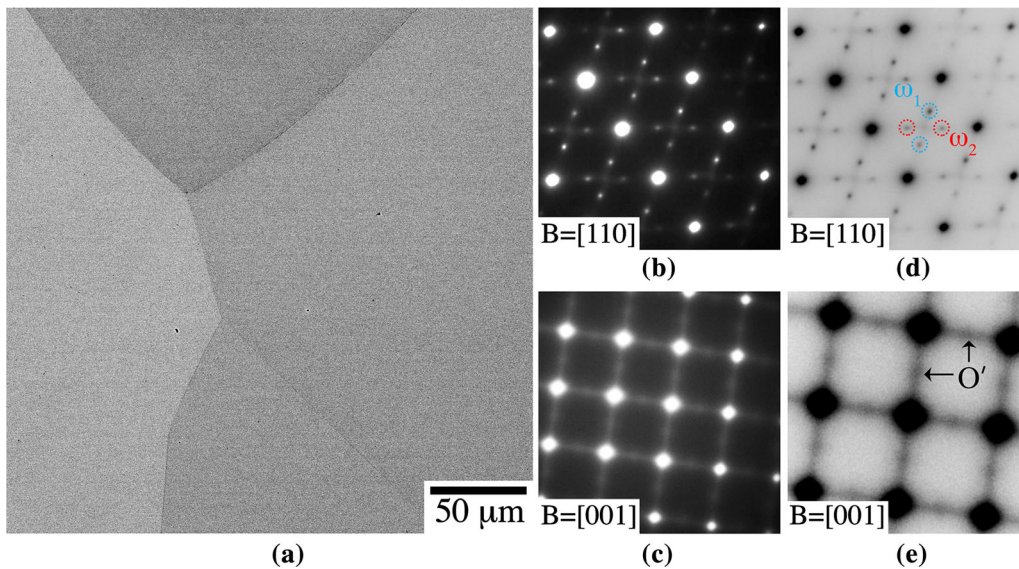
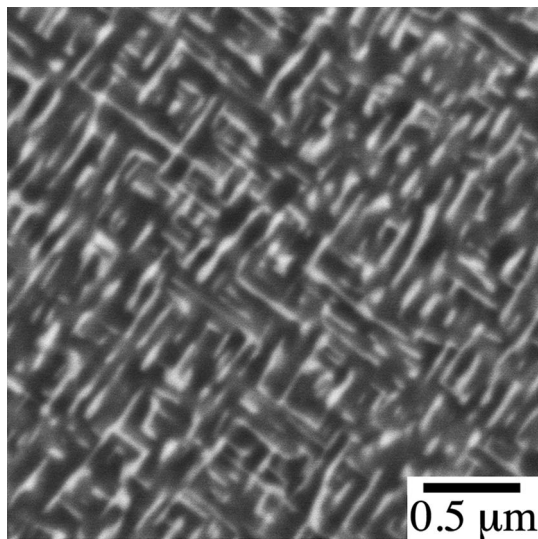


Fig. 12—(a) SEM BSE image of the microstructure of the alloy Ti64–3Fe following solution heat treatment at 1000 °C for 1 hour, followed by water quenching to room temperature. (b) and (c) Selected area diffraction patterns taken from within a grain of the heat-treated sample; beam directions are shown. (d) Variants of the omega phase may be discerned, depicted ω_1 (in turquoise) and ω_2 (in red), respectively. (e) The same diffraction pattern as in (c), but with the contrast reversed; diffraction maxima corresponding to the O' phase are indicated by the black arrows.

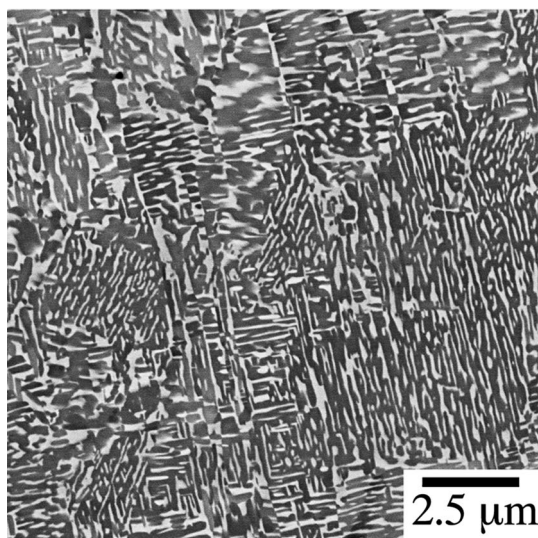
phase has been recently identified in metastable β alloys, for example, Ti5553.^[22] The change in alloy type from α/β to metastable β implies that heat treatments applied to such metastable alloys to develop very refined and uniform distributions of the α phase, and therefore very strong versions of Ti alloys, may also be used for Ti64–3Fe. To establish this possibility, samples of the solution heat-treated and quenched alloy have been aged for 1 hour at either 500 °C or 700 °C. The resultant microstructures are shown in Figure 13. Regarding the aging at 500 °C (Figure 13(a)), a very refined distribution of α laths is present. The identity of this phase and the absence of any intermetallic phase have been confirmed by using an aberration-corrected (S)TEM electron microscope, coupled with XEDS measurements. Thus, HAADF and bright-field images recorded in the (S)TEM are shown in Figures 14(a) and (b), respectively, and XEDS maps for the various elements noted on the figures are shown in Figures 14(c) through (f). From these measurements, the very refined second phase is shown to be the α phase. Using MIPAR software, image analysis has been used to quantify this latter microstructure, such that the volume fraction of the β phase is ≈ 24 pct, the average lath thickness is $\approx 0.06 \mu\text{m}$, and the areal density of laths is ≈ 37 laths μm^{-2} . The influence on this very refined distribution of the α phase on mechanical properties is considered below. For the sample aged at 700 °C, the microstructure is shown in Figure 13(b), and consists of a refined distribution of α plates, but on a somewhat coarser scale than that of the sample aged at 500 °C. Using MIPAR software, image analysis has been used to quantify this latter microstructure, such that the volume fraction of the β phase is ≈ 27 pct, the average lath thickness is $\approx 0.14 \mu\text{m}$, and the areal density of laths is ≈ 2 laths μm^{-2} .

A characteristic of microstructures in metastable β alloys is the ability to produce a variety of scales of α precipitation, from extremely refined, based on the details of α nucleation from the β phase.^[23] There are several possible nucleation processes that may be activated in metastable β Ti alloys, examples being the pseudo-spinodal mechanism, and heterogeneous nucleation involving the ω phase.^[24] In this previous work, nucleation leading to *refined* distributions with areal densities of α plates ≈ 1.5 laths μm^{-2} was attributed to a pseudo-spinodal mechanism, whereas in samples heated to produce *super-refined* distributions, with areal densities of α plates ≈ 40 laths μm^{-2} , it was concluded that the nucleation was influenced by the ω phase acting as a potent heterogeneous nucleation site. The refined distribution of the α phase in Ti64–3Fe following solution heat treatment, quenching and then up-quenching to 700 °C has an areal density of α plates being ≈ 2 laths μm^{-2} , and this is consistent with a mechanism such as the pseudo-spinodal being operative, followed by coarsening at the aging temperature. Furthermore, the ultrafine scale of the distribution of the α phase in Ti64–3Fe following solution heat treatment, quenching, and subsequent aging (500 °C) is consistent with the influence of the ω phase, the presence of which has been established in the as-quenched samples (Figure 12(b)), on the nucleation of the α phase. Thus, as noted above, the areal density for this alloy and heat treatment was measured to be ≈ 37 laths μm^{-2} , compared with a value of ≈ 40 laths μm^{-2} for ω -influenced nucleation of α laths in Reference 24 for the “super-refined” distribution in Ti5553.

It is interesting to note that a relatively small addition of Fe to Ti64 may change the nature of this alloy quite substantially, *i.e.*, from α/β to metastable β , whereas this is not the case for Ni additions. This difference in



(a)



(b)

Fig. 13—SEM BSE images of the microstructure of the alloy Ti64-3Fe following solution heat treatment at 1000 °C for 1 h, followed by water quenching to room temperature, and subsequently annealed at the following temperatures for 1 h. (a) 500 °C; (b) 700 °C.

behavior may be due to the potency of the alloying additions regarding the stability of the β phase. Thus, using the coefficients of the Mo equivalence^[21] for these two alloying additions to indicate their potency for β stability, the values are 1.25 and 2.9 for Ni and Fe, respectively. On this basis, it would be expected then that Fe is a much more effective element for stabilizing the β phase than is Ni, and so this may be a major factor in changing the nature of Ti64 to being a metastable β alloy when alloyed with sufficient additions of Fe. The difference in the morphology and scale of the α laths in LENSTM-deposited samples of the two alloys (Figure 9) may now be understood on the basis of the nature of this change in alloy type. For the Ni-containing alloy,

initially, the deposited microstructure would involve the formation of fine α laths accompanied by rejection of Ni into the surrounding β phase. It is reasonable to assume that during re-heating accompanying subsequent layer deposition, nucleation of the phase Ti_2Ni occurs reducing the concentration of Ni in the β solid solution which would reduce its stability, resulting in an increased volume fraction of the α phase, presumably accomplished by coarsening of the α laths. For the Fe-containing alloy, the microstructure is initially expected to consist of a very refined and uniform distribution of α laths; the scale of the distribution is expected to coarsen somewhat during temperature increases accompanying subsequent layer deposition while maintaining its uniformity. The phase $TiFe$ does not precipitate, and so the stability of the β phase is not changed, as is the case in the Ni-containing alloy.

D. Influence of Alloying Additions and Heat Treatments on Mechanical Response

Rockwell C hardness measurements have been used to provide a preliminary assessment of the mechanical response of the compositionally modified alloys as a function of heat treatment. The results are shown in Table II. As a basis of comparison, the typical values of Rockwell C hardness for Ti64 vary from ≈ 36 to 39, depending on the specifics of heat-treatment and, therefore, microstructure. Consider the results for the Ni containing alloy. In the LENSTM-deposited condition, the measured hardness value is 41. The microstructure is shown in Figure 9(a), and the hardness is presumably influenced by the presence of particles of the intermetallic compound Ti_2Ni and the Ni in solid solution at the solubility limit. Following solution heat treatment and water quenching to room temperature, the measured hardness of the alloy is 48. The microstructure is shown in Figure 10(a) and consists of refined plates of the α phase in a matrix of retained β . The increase in hardness is presumably due to the refined nature of the α phase distribution, and also to solid solution strengthening from the supersaturation of Ni in the retained β matrix. Aging these quenched samples at 450 °C for an hour yields a hardness value of 50; the corresponding microstructure is shown in Figure 11(a). The increase in hardness is attributed to the considerable precipitation of a refined distribution of α laths. For the solution treated and quenched alloy aged at 550 °C for an hour, the hardness remains at 50, which is an interesting result as the microstructure exhibits a coarser distribution of the α laths (Figure 11(b)). The expected decrease in hardness from the less refined distribution of α plates is probably compensated by the presence of the particles of Ti_2Ni .

Regarding the alloy Ti64-3Fe, the hardness of the LENSTM-deposited sample is 43, slightly higher than that of the Ni-containing alloy. This may be due to the presence of a more refined distribution of α plates (Figure 9(b)), as well as solid solution strengthening by Fe partitioning to the β phase (note that there is no evidence for precipitation of the equilibrium phase $TiFe$). In the solution-treated and water-quenched

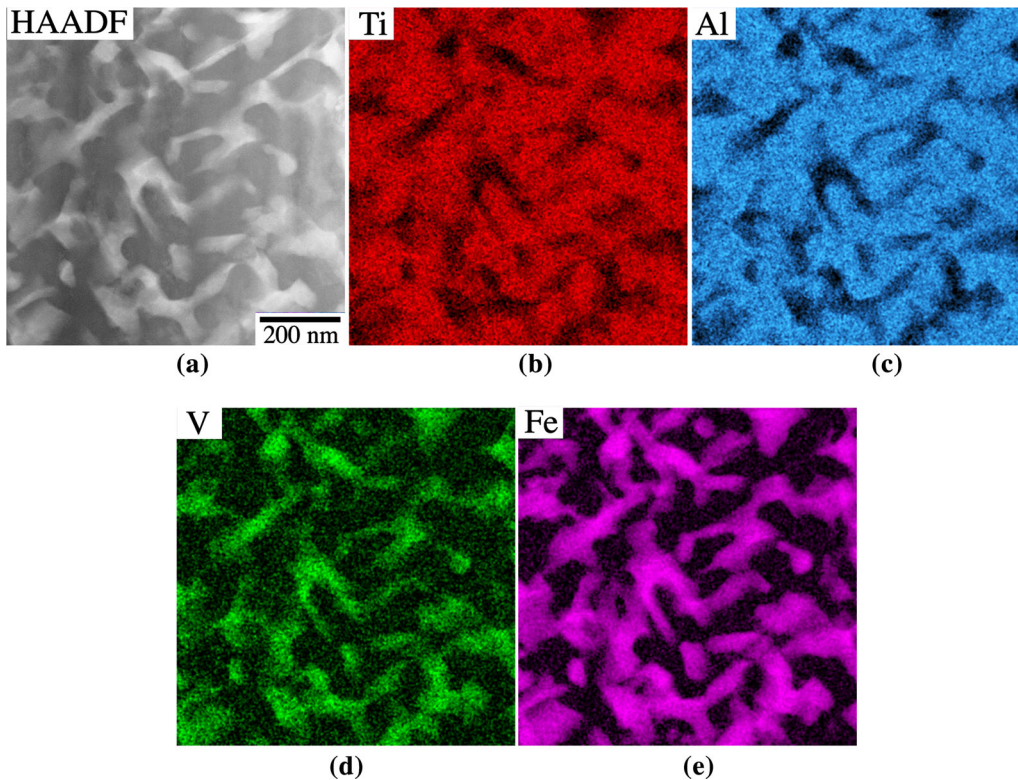


Fig. 14—STEM images of the microstructure of the alloy Ti64-3Fe following solution heat treatment at 1000 °C for 1 h, followed by water quenching to room temperature, and subsequently annealed at 500 °C for 1 h. (a) High-angle annular dark-field (HAADF) STEM image. (b) to (e) XEDS elemental maps, with the elements marked, recorded using a ChemiSTEM detector in an aberration-corrected Titan (S)TEM electron microscope.

Table II. Hardness Values (Rockwell C) for the Heat-Treated Alloys Listed (Compositions In Wt Pct)

Composition	Solution Heat treatment	Aging Temperature	Hardness (Rockwell C)
Ti64 + 3 pct Ni	As-deposited		41
Ti64 + 3 pct Ni	1000 °C—WQ	—	48
Ti64 + 3 pct Ni	1000 °C—WQ	450 °C	50
Ti64 + 3 pct Ni	1000 °C—WQ	550 °C	50
Ti64 + 3 pct Fe	As-deposited		43
Ti64 + 3 pct Fe	1000 °C—WQ	—	46
Ti64 + 3 pct Fe	1000 °C—WQ	500 °C	55
Ti64 + 3 pct Fe	1000 °C—WQ	700 °C	51

Typical values for Ti64 are 36–39 Rockwell C. The aging was for 1 h.

condition, the hardness is increased to 46. The microstructure consists of retained β , with a distribution of ω and O' phases (Figure 12); the increased hardness is attributed to solid solution strengthening of the retained β phase, and perhaps possible contributions from the metastable phases. When this solution-treated and quenched alloy is aged at 500 °C for an hour, the hardness is increased to 55, a very significant increase. The microstructure is shown in Figures 13(a) and 14(a) and (b), and consists of an extremely refined distribution of α precipitates. The hardness is attributed to this distribution, as well as solid solution strengthening of the β phase by Fe (which partitions to the β phase; there is no evidence of precipitation of TiFe). If the aging

treatment is performed at 700 °C (rather than 500 °C), the hardness drops to 51. This is consistent with the coarser distribution of the α plates, compared with those produced during the lower temperature age, as shown in Figure 13(b).

IV. SUMMARY

This paper has reported on the results of research focused on issues involving the use of alloying additions to optimize microstructures of high-performance Ti alloys processed by AM. The results may be summarized as follows.

1. Computational thermodynamics (CALPHAD) has been used to predict the effect of alloying additions on the freezing range of Ti alloys. It was predicted that alloying with Fe and Ni would increase the freezing range, and so a CET should occur during AM processing with the attendant rapid rates of cooling. This was confirmed experimentally. In contrast, additions of Mo are predicted to have only a very small influence on the freezing range, and so would not be expected to produce a CET during AM processing and this was also confirmed experimentally.
2. A method has been introduced for determining the minimum concentration of alloying addition required to effect a CET during AM processing. This involves the use of LENS™ to produce gradient builds of, for example, Ti64 with increasing amounts of Ni or Fe. For these two elements, the minimum concentration was found for both alloying additions to be ≈ 3 pct.
3. The gradient builds were also employed to demonstrate that while increasing the alloying additions above this minimum concentration results in a CET, subsequently reducing the concentration of alloying addition below that minimum reverses the transition and columnar microstructure results. This confirms that the change in microstructure is dependent only on the concentration of the given alloying addition, and not on other instrumental parameters.
4. It has been determined that the addition of 3 pctFe to the alloy Ti64 causes this alloy to change from an α/β Ti alloy to being a metastable β -Ti alloy, whereas additions of Ni do not produce the same result. This change in type of Ti alloy results in a marked difference in the development of microstructures of these compositionally modified alloys using heat treatments.
5. An initial assessment of the mechanical response through measurement of hardness (Table II) of these differences in microstructure has been made. The highest value of the hardness, 55 Rockwell C, was recorded from α sample of the alloy Ti64–3Fe, following quenching from above the β transus (1000 °C) and then aging at 500 °C. This may be compared with values for Ti64, which range from 36 to 39 Rockwell C.

ACKNOWLEDGMENTS

This research has been supported in part by the Titanium Metals Corporation and the Center for the Accelerated Maturation of Materials (OSU), and the authors gratefully acknowledge this support. Electron microscopy was performed at the Center for Electron Microscopy and Analysis (CEMAS) at The Ohio State University, and the authors are grateful for the provision of these facilities.

CONFLICT OF INTEREST

On behalf of all authors, the corresponding author states that there is no conflict of interest.

OPEN ACCESS

This article is licensed under a Creative Commons Attribution 4.0 International License, which permits use, sharing, adaptation, distribution and reproduction in any medium or format, as long as you give appropriate credit to the original author(s) and the source, provide a link to the Creative Commons licence, and indicate if changes were made. The images or other third party material in this article are included in the article's Creative Commons licence, unless indicated otherwise in a credit line to the material. If material is not included in the article's Creative Commons licence and your intended use is not permitted by statutory regulation or exceeds the permitted use, you will need to obtain permission directly from the copyright holder. To view a copy of this licence, visit <http://creativecommons.org/licenses/by/4.0/>.

SUPPLEMENTARY INFORMATION

The online version contains supplementary material available at <https://doi.org/10.1007/s11661-021-06475-3>.

REFERENCES

1. N. Guo and M.C. Leu: *Front. Mech. Eng.*, 2013, vol. 8, pp. 215–43.
2. E. Uhlmann, R. Kersting, T.B. Klein, M.F. Cruz, and A.V. Borille: *Procedia CIRP*, 2015, vol. 35, pp. 55–60.
3. Y. Zhai, H. Galarraga, and D.A. Lados: *Eng. Failure Anal.*, 2016, vol. 69, pp. 3–14.
4. A.A. Antonysamy, J. Meyer, and P.B. Prangnell: *Mater. Charact.*, 2013, vol. 84, pp. 153–68.
5. X. Wu, J. Liang, J. Mei, C. Mitchell, P.S. Goodwin, and W. Voice: *Mater. Des.*, 2004, vol. 25, pp. 137–44.
6. M.M. Kirka, Y. Lee, D.A. Greeley, A. Okello, M.J. Goin, M.T. Pearce, and R.R. Dehoff: *JOM*, 2017, vol. 69, pp. 523–31.
7. J.H. Martin, B.D. Yahata, J.M. Hundley, J.A. Mayer, T.A. Schaedler, and T.M. Pollock: *Nature*, 2017, vol. 549, pp. 365–69.
8. P. Barriobero-Vila, J. Gussone, A. Stark, N. Schell, J. Haubrich, and G. Requena: *Nat. Commun.*, 2018, vol. 9, pp. 3426–35.
9. M.J. Bermingham, S.D. McDonald, and M.S. Dargusch: *Mater. Sci. Eng. A*, 2018, vol. 719, pp. 1–11.
10. P. Barriobero-Vila, J. Gussone, A. Stark, N. Schell, J. Haubrich, and G. Requena: *Nat. Commun.*, 2018, vol. 9, pp. 1–9.
11. J.D. Hunt: *Mater. Sci. Eng. A*, 1984, vol. 65, pp. 75–83.
12. W. Kurz, C. Bezencon, and M. Gaumann: *Sci. Technol. Adv. Mater.*, 2001, vol. 2, pp. 185–91.
13. B.A. Welk and H.L. Fraser: U.S. Provisional Application No. 62/463,338, 2017.
14. D. Zhang, D. Qui, M. Gibson, Y. Zheng, H.L. Fraser, D. StJohn, and M. Easton: *Nature*, 2019, vol. 576, pp. 91–95.
15. M.J. Bermingham, S.D. McDonald, D.H. StJohn, and M.S. Dargusch: *J. Alloys Compd.*, 2009, vol. 481, pp. 20–23.

16. M. Simonelli, D. McCartney, P. Barriobero-vila, N. Aboulkhair, Y. Tse, A. Clare, and R. Hague: *Metall. Mater. Trans. A*, 2020, vol. 51A, pp. 2444–59.
17. M.Y. Mendoza, P. Samimi, D.A. Brice, B. Martic, M. Rolchigo, R. LeSar, and P.C. Collins: *Metall. Mater. Trans. A*, 2017, vol. 48A, pp. 3594–05.
18. A.L. Pilchak and J.C. Williams: *Metall. Mater. Trans. A*, 2011, vol. 42A, pp. 773–94.
19. K.I. Schwendner, R. Banerjee, P.C. Collins, C.A. Brice, and H.L. Fraser: *Scr. Mater.*, 2001, vol. 45, pp. 1123–29.
20. L. Scotti, N. Warnken, and A. Mottura: *Acta Mater.*, 2019, vol. 177, pp. 68–81.
21. G. Lutjering and J. Williams: *Titanium*, 2nd ed., Springer, New York, 2007, pp. 15–52.
22. Y. Zheng, R. Williams, D. Wang, R. Shi, S. Nag, P. Kami, J. Sosa, R. Banerjee, Y. Wang, and H. Fraser: *Acta Mater.*, 2016, vol. 103, pp. 850–58.
23. S. Nag, Y. Zheng, R. Williams, A. Devajar, A. Boyne, Y. Wang, P. Collins, G. Viswanathan, J. Tiley, B. Muddle, R. Banerjee, and H. Fraser: *Acta Mater.*, 2012, vol. 60, pp. 6247–56.
24. Y. Zheng, R. Williams, J. Sosa, A. Talukder, Y. Wang, R. Banerjee, and H. Fraser: *Acta Mater.*, 2016, vol. 103, pp. 165–73.

Publisher's Note Springer Nature remains neutral with regard to jurisdictional claims in published maps and institutional affiliations.